Progress In Electromagnetics Research M, Vol. 39, 151–159, 2014

Automatic Target Recognition Using Jet Engine Modulation and Time-Frequency Transform

Sang-Hong Park*

Abstract—We propose a method to recognize targets by using the signature of jet engine modulation (JEM) generated by the rotating blades in jet engines. The method combines time-frequency transform, 2-dimensional (2D) principal component analysis, and a nearest-neighbor classifier. In simulations using five propellers composed of isotropic point scatterers, the proposed method was insensitive to signal-to-noise SNR variation; this insensitivity was a result of the effective 2D time-frequency feature and the noise suppression by the matched filter. In simulations using a reduced training database, the result was most sensitive to variation in the rotation velocity of the blades.

1. INTRODUCTION

Automatic target recognition (ATR) is a technique to detect and recognize a target by using data collected from a variety of radar sensors that use wide-band electromagnetic signals. ATR has been widely applied to classification of enemy jets in warfare. Mainly, two features have been used for ATR: high resolution range profile (HRRP) and inverse synthetic aperture radar image (ISAR). However, recent research results indicate that another signature called the micro-Doppler (m-D) phenomenon [1] has high potential for use in ATR [2].

The basic principle for m-D is that rapid mechanical rotation and vibration components of a rigid body impose additional Doppler frequency modulation on the returned radar signal. The amount of frequency modulation is $f_D = 2v/\lambda$ where v is the relative velocity of the blade to the radar line of sight and λ the wavelength of the radar signal. For the ISAR image, this frequency modulation seriously blurs the image in cross-range direction (Figure 1), and therefore should be removed to enable ATR of the ISAR image. However, these noise-like components can also be exploited for ATR as a useful signature because they represent the time-varying frequency of the target.

m-D has been applied to target recognition. High-resolution time-frequency techniques can be used to extract the time-varying m-D signature [3]. The adaptive chirplet presentation can extract the m-D signature from an ISAR image of an aircraft [4] and image-processing algorithms such as the Radon transform [5] and the Hough transform (HT) [6] have been introduced to separate m-D features m-D analysis has been used to classify the type of helicopter blade [5] or automobile wheel [7], to analyze human gaits and wind farms [8, 9]. Recently, MD has been intensively applied to the recognition of the ballistic missile [10, 11].

The rotation of blades in a jet produces engine modulation (JEM) [2]. Each fighter jet is equipped with a unique engine that provides a distinct JEM signature that can used for ATR. In this paper, by using the mathematical modeling and the obtained characteristics of JEM, we identify a target based on time-frequency transform (TFT) and two-dimensional (2D) principle component analysis (PCA). A training database was constructed for each of the numerous regular increments of the aspect angle and the rotational velocity (RV). The test data were obtained at a random angle and a random RV. Then classification was conducted using a nearest neighbor classifier and a time-frequency signature

Received 7 October 2014, Accepted 2 November 2014, Scheduled 6 November 2014
* Corresponding author: Sang-Hong Park (radar@pknu.ac.kr).
The author is with the Department of Electronic Engineering, Pukyong National University, Busan, Korea.

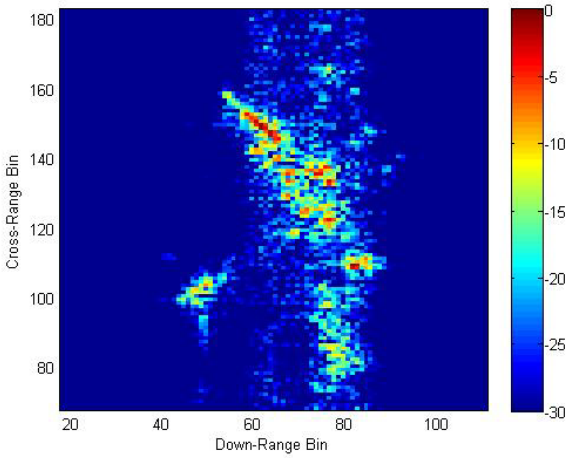

Figure 1. ISAR image of a Boeing747 contaminated by micro-Doppler frequency modulation.

compressed by 2D PCA. In simulations using five different propellers composed of isotropic point scatterers, the proposed method yielded high classification results even at low SNRs due to the effective 2D time-frequency feature.

2. MATHEMATICAL MODELING AND PROPOSED METHOD

2.1. Mathematical Modeling of JEM

Consider that a propeller composed of point scatters is placed on the y-axis and rotating around it at RV ω_R. The position of scatterer s on blade b in the propeller at slow-time t_p is given by

$$\begin{bmatrix} x\left(t_p\right)_{bs} \\ y\left(t_p\right)_{bs} \\ z\left(t_p\right)_{bs} \end{bmatrix} = \begin{bmatrix} \cos\left(\omega_R t_p + \phi_0\right) & 0 & -\sin\left(\omega_R t_p + \phi_0\right) \\ 0 & 1 & 0 \\ \sin\left(\omega_R t_p + \phi_0\right) & 0 & \cos\left(\omega_R t_p + \phi_0\right) \end{bmatrix} \begin{bmatrix} x_{0bs} \\ y_{0bs} \\ z_{0bs} \end{bmatrix} + \begin{bmatrix} 0 \\ y_{cen} \\ 0 \end{bmatrix}, \tag{1}$$

where $[x_{0bs}\ y_{0bs}\ z_{0bs}]^T$ is the initial position of the scatterer, $[0\ y_{cen}\ 0]^T$ the position of the propeller center, and ϕ_0 the initial angle of the blade. Slow time is expressed in terms of the radar pulse repetition interval (PRI) and is different from the fast time t for the radar signal. If the scatter is seen at an aspect angle θ to its local (x, y) coordinate, (1) becomes

$$\begin{bmatrix} x\left(t_p\right)_{\theta bs} \\ y\left(t_p\right)_{\theta bs} \\ z\left(t_p\right)_{\theta bs} \end{bmatrix} = \begin{bmatrix} \cos\theta & -\sin\theta & 0 \\ \sin\theta & \cos\theta & 0 \\ 0 & 0 & 1 \end{bmatrix} \begin{bmatrix} \cos\left(\omega_R t_p + \phi_0\right) & 0 & -\sin\left(\omega_R t_p + \phi_0\right) \\ 0 & 1 & 0 \\ \sin\left(\omega_R t_p + \phi_0\right) & 0 & \cos\left(\omega_R t_p + \phi_0\right) \end{bmatrix} \begin{bmatrix} x_{0bs} \\ y_{0bs} \\ z_{0bs} \end{bmatrix} + \begin{bmatrix} 0 \\ y_{cen} \\ 0 \end{bmatrix}, \tag{2}$$

where $[x(t_p)_{\theta bs}\ y(t_p)_{\theta bs}\ z(t_p)_{\theta bs}]^T$ is the position of the scatterer at the an angle θ.

Assuming the plane wave approximation and the radar line of sight (RLOS) vector [0 1 0], the distance to s on b at t_p and θ is given by

$$\begin{aligned} r\left(t_p\right)_{\theta bs} = y\left(t_p\right)_{\theta bs} = {} & x_{0bs}\cos\left(\omega_R t_p + \phi_0\right)\sin\theta - z_{0bs}\sin\left(\omega_R t_p + \phi_0\right)\sin\theta + y_{cen} + y_{0bs}\cos\theta \\ & + x_{0bs}\sin\left(\omega_R t_p + \phi_0\right) + z_{0bs}\cos\left(\omega_R t_p + \phi_0\right), \end{aligned} \tag{3}$$

which is a simple inner product of the RLOS vector and position vector. Then, the echo signal $s_R(t)$ of the transmitted radar signal with frequency f becomes

$$s_R\left(t_p\right) = \exp\left[j2\pi f\left(t - \frac{2r\left(t_p\right)_{\theta bs}}{c}\right)\right] = \exp\left[j2\pi f_0 t + \Phi\left(t_p\right)_{\theta bs}\right], \quad \text{where} \quad \Phi\left(t_p\right)_{\theta bs} = -\frac{4\pi r\left(t_p\right)_{\theta bs}}{\lambda}. \tag{4}$$

After baseband conversion, the frequency at t caused by the rotating scatter becomes

$$f\left(t_p\right)_{\theta bs} = \frac{d\Phi(t_p)_{\theta bs}}{dt_p} = -\frac{4\pi}{\lambda}\left(\omega_R\cos(\omega_R t_p + \phi_0)(x_{0bs} - z_{0bs}\sin\theta) - \omega_R\sin(\omega_R t_p + \phi_0)(x_{0bs}\sin\theta + z_{0bs})\right), \tag{5}$$

which is the sum of the sine and cosine functions of ω_R. Thus, a time-frequency method is more efficient to describe the time-varying nature of JEM than is a simple FT method.

2.2. Rada Signal Modeling

For the radar signal, we assume a monostatic chirp waveform [12]

$$r(t) = A_0 e^{j2\pi\left(f_0 t + \frac{B_w t^2}{2\tau}\right)} \times rect\left(\frac{t}{\tau}\right), \tag{6}$$

where $r(t)$ is a transmitted signal at t, A_0 its amplitude, f_0 the start frequency, B_w the bandwidth, τ the pulse duration, and $rect = 1$ if $t - \tau/2 \leq t \leq t + \tau/2$ and 0 otherwise. At each pulse emission time t_p, the received signal reflected from a propeller composed of B blades, each of which has S isotropic point scatterers, becomes

$$g\left(t_p, t\right) = \sum_{b=1}^{B}\sum_{s=1}^{S} A_{bs} e^{j2\pi\left(f_0(t - r(t_p)_{bs}) + \frac{B_w\left(t - r(t_p)_{bs}\right)^2}{2\tau}\right)} \times rect\left(\frac{t - r(t_p)_{bs}}{\tau}\right), \tag{7}$$

where A_{bs} is the amplitude of s in b, $r(t_p)_{bs}$ the time delay between the radar and the scatterer at t_p, and $r(t_p)_{bs}$ is calculated using a plane wave approximation, in which the distance to a scattering center is that projected onto the RLOS vector. The discrete expression for (7) is

$$g[m, n] = \sum_{b=1}^{B}\sum_{s=1}^{S} A_{bs} e^{j2\pi\left(f_0(nT_s - r(mT)_{bs}) + \frac{B\left(nT_s - r(mT)_{bs}\right)^2}{2\tau}\right)} \times rect\left(\frac{nT_s - r(mT)_{bs}}{\tau}\right), \tag{8}$$

where T_s is the sampling period for the radar, T the pulse repetition interval (PRI), m is a fast-time index, and n a slow-time index. The time-varying frequency of the JEM is sampled at the pulse repetition frequency (PRF) equal to 1/PRI, so high PRFs are required when sampling high JEM frequencies.

2.3. TFT and 2D PCA

TFT is used to represent the power distribution of the frequency of JEM over time. In this paper, we use the short-time Fourier transform (STFT) which is easily implemented by the simple fast FT. The input signal $s(t)$ at time τ is transformed by STFT to [13]:

$$STFT\left(t, f\right) = \int_{-\infty}^{\infty} s\left(\tau\right)\gamma^*\left(\tau - t\right) e^{-j2\pi f\tau} d\tau, \tag{9}$$

where f is the frequency and γ the window function. Because the sidelobe caused by the rectangular window may distort the MD image, we used the window function at the cost of increased resolution. In this paper, Hamming window was used. Other types of windows such as Hanning, Blackman, and spline windows can be used depending on the TFT method. In discrete form, (9) is expressed as

$$STFT[p, q] = \sum_{k=0}^{L-1} s[k]\gamma\left[k - p\right] e^{-\frac{2\pi qk}{L}}, \tag{10}$$

where k is the time index, L the window length, p sampled time index, and q the sampled frequency index.

Because the TFT image contains much redundant information, we apply 2D PCA to compress the image and to extract useful features that distinguish targets effectively. The main point of 2D PCA is to use a simple matrix multiplication

$$\mathbf{Y} = \mathbf{AX}, \tag{11}$$

to project the TFT image $\mathbf{A}$ onto the projection axes $\mathbf{X}$, where $\mathbf{X}$ is a set of d eigenvectors of the image covariance matrix given by

$$\mathbf{G}_t = \frac{1}{M_{tr}} \sum_{j=1}^{M_{tr}} \left(\mathbf{A}_j - \bar{\mathbf{A}}\right)^T \left(\mathbf{A}_j - \bar{\mathbf{A}}\right), \tag{12}$$

where M_{tr} is the number of the training images, and $\bar{\mathbf{A}}$ is the average of the training images. Then, a $P \times Q$ image is compressed into the $P \times d$ image (detailed procedure is in [14]).

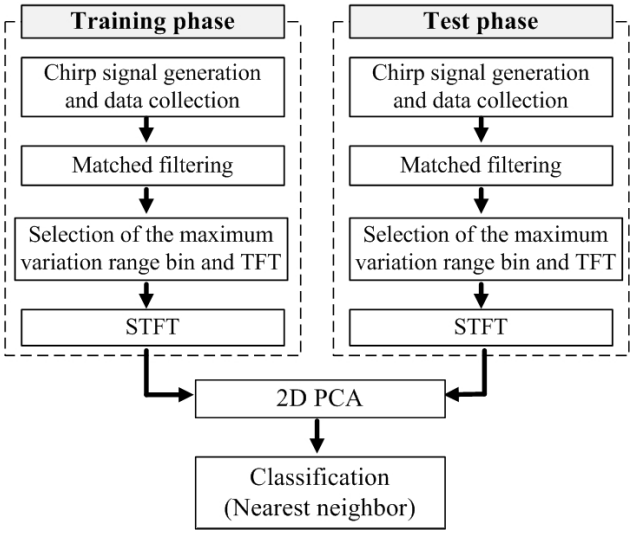

Figure 2. Proposed classification procedure.

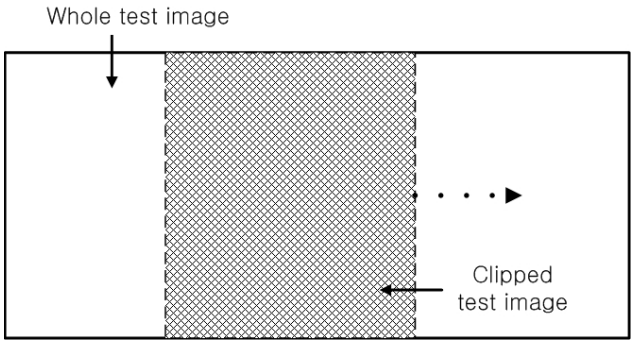

Figure 3. Test image clipping.

2.4. Proposed Recognition Method

The proposed method is composed a training phase and a test phase (Figure 2). In each phase, the collected radar signal in (8) is matched-filtered for each m to yield HRRP (Figure 2). To automatically select the range bin of JEM, we used the variation of the absolute value in the HRRP and selected the one that yielded the highest variation. Because the initial phases of the sinusoidal curve can differ between the training data and the test data, the test data require longer observation time to find the maximum match than do the training data.

In the second step, STFT is conducted using the signal in the selected range bin to construct the training and test TFT images. Due to the longer observation time for the data, the test TFT image has a longer time axis than the training TFT image when the frequency axes are equal. In classification, the training and test images are compressed by 2D PCA, and the test image is classified by a simple nearest neighbor whose classification rule is as follows:

$$\hat{i} = \min_i \|\mathbf{Y}_u - \mathbf{Y}_i\|, \tag{13}$$

where $\mathbf{Y}_u$ is the compressed 2D PCA image of an unknown target, and $\mathbf{Y}_i$ is that of the training image of the ith target, and $\|\cdot\|$ is the Frobenius norm [15]. The Frobenius norm of a $m_a \times n_a$ matrix $\mathbf{A}$ is given by

$$\|\mathbf{A}\| = \sqrt{\sum_{i=1}^{m_a}\sum_{j=1}^{n_a}|a_{ij}|^2}. \tag{14}$$

Because of the size difference between the training and test images, the test TFT image is clipped using a window with the training image size, shifting from the 1st column of the test image to the last (Figure 3). For each shift a, the clipped image is divided by $\|\mathbf{A}\|$ (14) to remove the amplitude variation, then 2D PCA is applied to derive $\mathbf{Y}_{ua}$ and $\|\mathbf{Y}_{ua} - \mathbf{Y}_i\|$. Finally, the minimum value of $\|\mathbf{Y}_{ua} - \mathbf{Y}_i\|$ is used as $\|\mathbf{Y}_u - \mathbf{Y}_i\|$ for the ith target.

3. SIMULATION RESULT

In simulations we used five propellers consisting of isotropic point scatterers (Figure 4). To examine a difficult condition, targets 1 and 2 were set to have the same number of propellers with different numbers of scatterers (Figures 4(a), (b)), as were targets 3 and 4 (Figures 4(c), (d)). For the radar system, we used a monostatic chirp radar with pulse repetition frequency = 2 kHz, center frequency = 9.15 GHz, $B_w = 200$ MHz, sampling frequency = 512 MHz and $\tau_p = 30\,\mu$s.

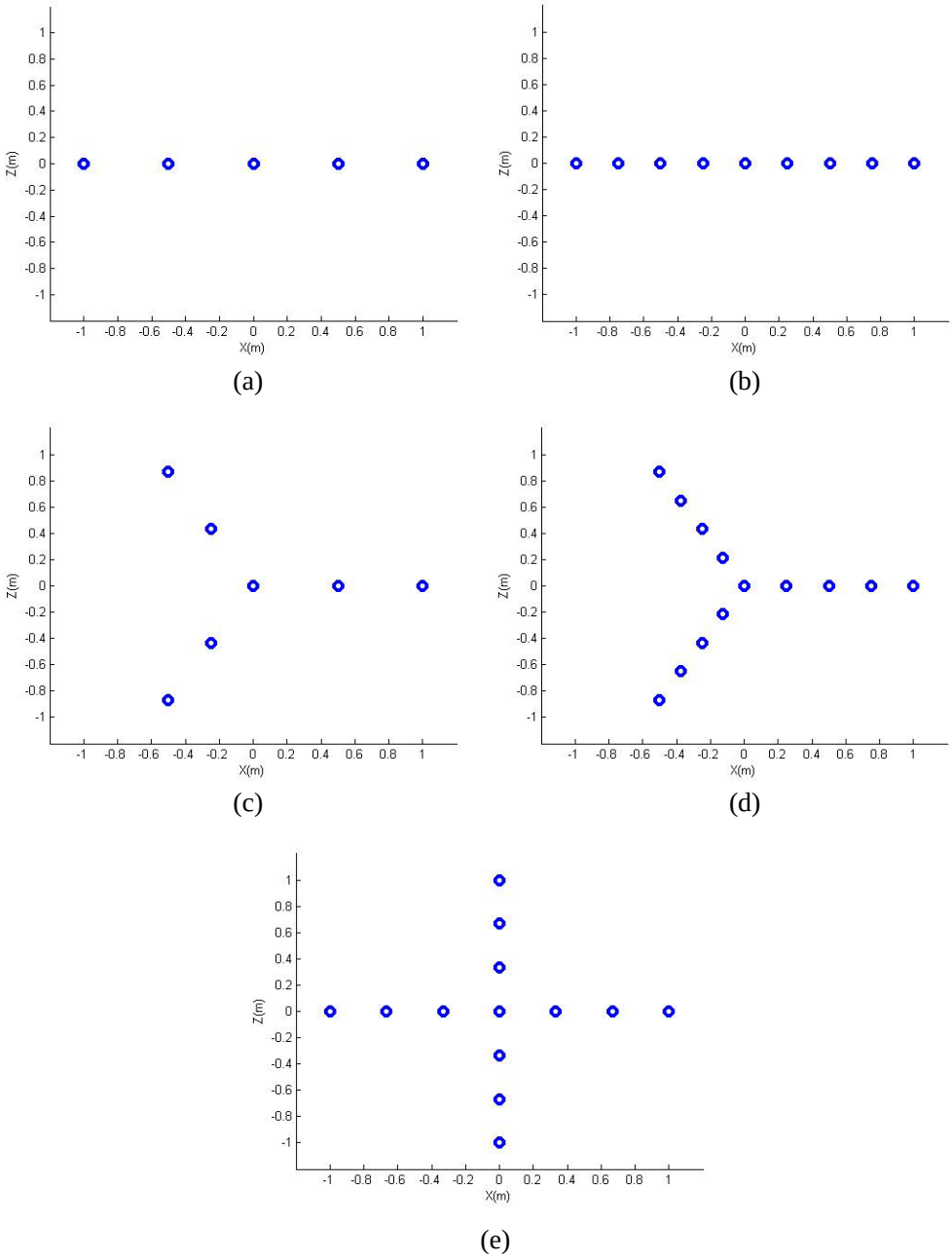

Figure 4. Propeller targets used for simulation. (a) Target 1. (b) Target 2. (c) Target 3. (d) Target 4. (e) Target 5.

The radar was placed at the origin, and each target was placed at [0 10 0] km, facing the radar, and was observed for 10 s during the training phase and for 20 s during the test phase. The training database was constructed by uniformly sampling the aspect angle in increments of $\Delta\theta$ in an angular range of 0∼70°, over which JEM of the target is known to be seen by the radar [16]. The RV was measured in revolutions per minute (RPM) with 1 RPM $= 2\pi$ rads/(60 s) $= 0.0525$ rad/s (see (2) for θ and ω_R). For each sampled aspect angle, the RVs were sampled in increments of ΔRPM in a range of 3∼7 RPMs. To study the effect of the training database reduction, $\Delta\theta$ and ΔRPM were varied. Then 50 test data per target were collected at a random angle and a random RPM in the ranges, yielding a total of 250 test images. To simulate the effect of noise, additive white Gaussian noise was added to the test data

to achieve the desired signal-to-noise ratio (SNR). d for 2D PCA in (11) was set to 2 because this value gives good classification results [17]. Classification accuracy was expressed as the correct classification percentage

$$P_c = M_c/M_{tr} \times 100\%, \tag{15}$$

where M_c is the number of correct classifications, and M_{tr} is the same as in (12).

In constructing TFT images from the sampled JEM data in a range bin with the maximum signal variation, the 50-point Hamming window was used with an overlap of 40 points between each pair of neighboring time samples. Each 50-point set of windowed data was zero-padded to 2048 points, and fast FT was conducted to construct the TFI for each time shift.

The TFT images of targets at $\theta = 30^\circ$ and rotating at RPM = 7 consisted of sinusoidal waves

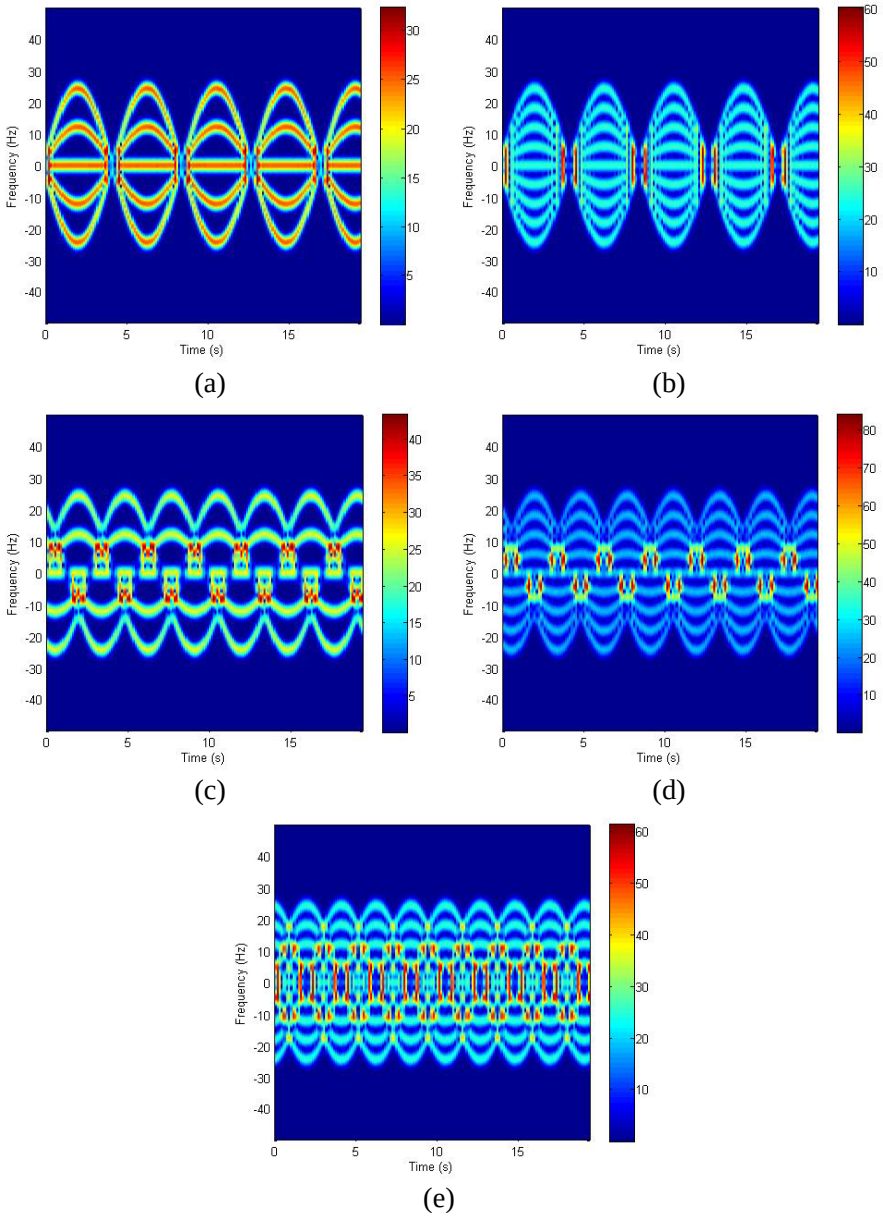

Figure 5. TFT image of JEM signal in each target ($\theta = 30$, RPM = 7). (a) Target 1. (b) Target 2. (c) Target 3. (d) Target 4. (e) Target 5.

caused by the rotation of each scatterer (Figure 5). Each wave had an amplitude that corresponded to the distance of the scatterer from the center, and phases of the waves were offset by an amount that corresponded to the angle between pairs of blades; i.e., a constant line (amplitude 0) for the central scatterer, and two or four additional waves offset by 180° (Target 1, Figure 5(a); Target 2, Figure 5(b)), 120° (Target 3, Figure 5(c); Target 4, Figure 5(d)), or 90° (Target 5, Figure 5(e)).

The simulation result for various SNRs (0∼30 dB with 10 dB increment) with $\Delta\theta = 1°$ and $\Delta RPM = 1$ was very stable and degraded as SNR decreased (Figure 6). However, the degree of degradation was very small (P_c remained $> 95\%$) because of noise suppression by the matched-filter. The effective 2D features of the TFI image also contributed to the high P_c at low SNR. This result proves that JEM can be very effective for ATR.

In simulations using $1 \leq \Delta\theta \leq 10$ in increments of 1 with SNR = 30 dB and $\Delta RPM = 1$, the result was more sensitive to variation of $\Delta\theta$ than to variation of SNR (Figure 7). Due to the reduced size of the training database, P_c decreased as $\Delta\theta$ increased. P_c was 89.2% for $\Delta\theta \geq 5°$, so $\Delta\theta$ should be $< 5°$ to achieve $P_c > 90\%$.

P_c was most sensitive to ΔRPM variation as it was varied from 1 to 5 with an increment 1 with $\Delta\theta = 1°$ and SNR = 30 dB. The sharp degradation in P_c (Figure 8) was due to the scaling of the sinusoidal curves in the TFT image. Because the sinusoidal curves in the TFT image can be scaled or expanded depending on the RPM, the result was most affected by RPM. The simulations suggest that ΔRPM should be < 3 (50% of the total RPM range) to achieve $P_c > 90\%$. However this value of ΔRPM is not absolute because at very high RPMs, this small ΔRPM would not considerably affect the

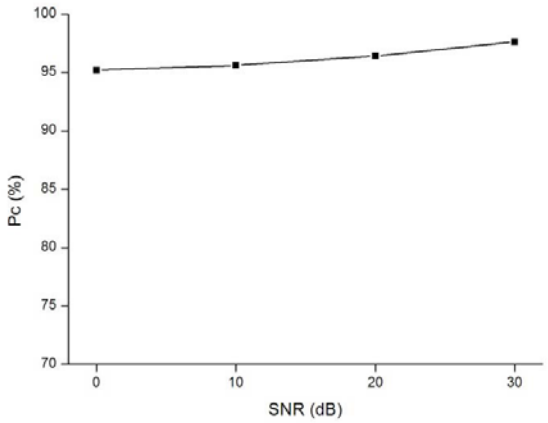

Figure 6. Percent correct identification vs. SNRs.

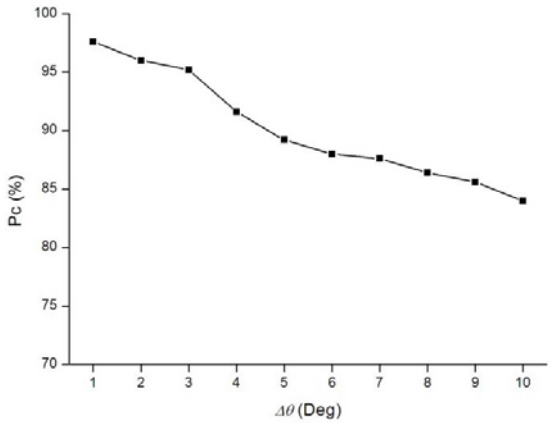

Figure 7. Percent correct identification vs. $\Delta\theta$.

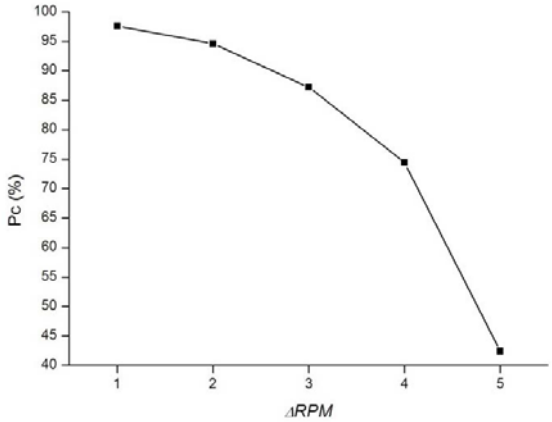

Figure 8. Percent correct identification vs. ΔRPM.

shape of a TFI image; further investigations using several RPM ranges should be conducted to define this range more definitively.

4. CONCLUSION

We proposed an efficient method composed of range compression, TFT, 2D PCA and the nearest neighbor classifier to recognize targets using their JEM signatures. The time-varying frequency of JEM signal due to the rotation of the propeller was proved by the signal model, and high classification accuracy was obtained in simulations using five propeller models that consisted of isotropic scatterers. The simulation result was insensitive to SNR variation and was sensitive to $\Delta\theta$ and ΔRPM; the result was more dependent on ΔRPM than on $\Delta\theta$ due to the variation of sinusoidal curves in the TFT image. For ΔRPM, further investigations are required using several RPM ranges.

This paper provides strong evidence that the JEM signature can be applied to ATR to identify jets. However, it should not be used alone, but used with other features such as 2D ISAR image. When the aircraft closes directly toward the radar, ISAR image cannot provide useful features for ATR because of the high elevation angle [18]. In this case, the JEM signal collected from the observed propeller will significantly improve the classification result. Our next research will focus on fusion of the two features when a jet moves directly toward the radar.

ACKNOWLEDGMENT

This research was supported by Basic Science Research Program through the National Research Foundation of Korea (NRF) funded by the Ministry of Education, Science and Technology (2012R1A1A1002047).

REFERENCES

1. Chen, V. C., F. Li, S. S. Ho, and H. Wechsler, "Micro-Doppler effect in radar: Phenomenon, model, and simulation study," *IEEE Trans. Aerosp. Electron. Syst.*, Vol. 42, No. 1, 2–21, Jan. 2006.
2. Tait, P., *Introduction to Radar Target Recognition*, IET, 2005.
3. Thayaparan, T., S. Abrol, E. Riseborough, L. Stankovic, D. Lamothe, and G. Duff, "Analysis of radar micro-Doppler signatures from experimental helicopter and human data," *IET Radar Sonar Navig.*, Vol. 1, No. 4, 289–299, Aug. 2007.
4. Li, J. and H. Ling, "Application of adaptive chirplet representation for ISAR feature extraction from targets with rotating parts," *Proc. Inst. Elect. Eng. Radar Sonar Navig.*, Vol. 150, No. 4, 284–291, Aug. 2003.
5. Stankovic, L., I. Djurovic, and T. Thayaparan, "Separation of target rigid body and micro-Doppler effects in ISAR imaging," *IEEE Trans. Aerosp. Electron. Syst.*, Vol. 42, No. 4, 1496–1506, Oct. 2006.
6. Zhang, Q., T. S. Yeo, H. S. Tan, and Y. Luo, "Imaging of a moving target with rotating parts based on the Hough transform," *IEEE Trans. Geosci. Remote Sens.*, Vol. 46, No. 1, 291–299, Jan. 2008.
7. Ghaleb, A., L. Vignaud, and J. M. Nicolas, "Micro-Doppler analysis of wheels and pedestrians in ISAR imaging," *IET Signal Process.*, Vol. 2, No. 3, 301–311, Sep. 2008.
8. Kim, Y. and H. Ling, "Human activity classification based on micro-Doppler signatures using a support vector machine," *IEEE Trans. Geosci. Remote Sens.*, Vol. 47, No. 5, 1328–1337, May 2009.
9. Jung, J. H., U. Lee, S. H. Kim, and S. H. Park, "Micro-Doppler analysis of Korean offshore wind turbine on the L-band radar," *Progress In Electromagnetics Research*, Vol. 143, 87–104, 2010.
10. Jung, J. H., K. T. Kim, S. H. Kim, and S. H. Park, "Micro-Doppler extraction and analysis of the ballistic missile using RDA based on the real flight scenario," *Progress In Electromagnetics Research M*, Vol. 37, 83–93, 2014.
11. Liu, L., D. Mclernon, M. Ghogho, W. Hu, and J. Huang, "Ballistic missile detection via micro-Doppler frequency estimation from radar return," *Digital Signal Processing*, Vol. 22, 87–95, 2012.
12. Mahafza, B. R., *Radar Systems Analysis and Design Using MATLAB*, CRC Press LLC, 2000.

13. Qian, S., *Time-freqency and Wavelet Transforms*, Prentice Hall PTR, 2002.
14. Yang, J., D. Zhang, A. F. Frangi, and J.-Y. Yang, "Two-dimensional PCA: A new approach to appearance-based face representation and recognition," *IEEE Trans. Pattern Analysis and Machine Intelligence*, Vol. 26, 131–137, Jan. 2004.
15. Golub, G. H. and C. F. Van Loan, *Matrix Computations*, The Johns Hopkins University Press, 1996.
16. Zyweck, A., "Preprocessing issues in high resolution radar target classification," Ph.D. Thesis, University of Adelaide, Australia, 1995.
17. Han, S.-K., H.-T. Kim, S.-H. Park, and K.-T. Kim, "Efficient radar target recognition using a combination of range profile and time-frequency analysis," *Progress In Electromagnetics Research*, Vol. 108, 131–140, 2010.
18. Park, S.-H., M.-G. Joo, and K.-T. Kim, "Construction of ISAR training database for automatic target recognition," *Journal of Electromagnetic Waves and Applications*, Vol. 25, Nos. 11–12, 1493–1503, 2011.